

Low-temperature one-step solid-phase synthesis of carbon-encapsulated TiO_2 nanocrystals as anode materials for lithium-ion batteries

Boyang Liu¹ · Yingfeng Shao² · Xin Xiang¹ · Jiayuan Ren¹ · Wenge Li³

Received: 14 September 2016 / Revised: 27 February 2017 / Accepted: 27 February 2017 / Published online: 9 March 2017
© Springer-Verlag Berlin Heidelberg 2017

Abstract A simple and highly efficient method is developed for in situ one-step preparation of carbon co-encapsulated anatase and rutile TiO_2 nanocrystals ($\text{TiO}_2@\text{C}$) with core-shell structure for lithium-ion battery anode. The synthesis is depending on the solid-phase reaction of titanocene dichloride with ammonium persulfate in an autoclave at 200 °C for 30 min. The other three titanocene complexes including bis(cyclopentadienyl)dicarbonyl titanium, cyclopentadienyltitanium trichloride, and cyclopentadienyl(cycloheptatrienyl)titanium are used instead to comprehensively investigate the formation mechanism and to improve the microstructure of the product. The huge heat generated during the explosive reaction cleaves the cyclopentadiene ligands into small carbon fragments, which form carbon shell

after oxidative dehydrogenation coating on the TiO_2 nanocrystals, resulting in the formation of core-shell structure. The TiO_2 nanocrystals prepared by titanocene dichloride have an equiaxed morphology with a small diameter of 10–55 nm and the median size is 30.3 nm. Hundreds of TiO_2 nanocrystals are encapsulated together by the worm-like carbon shell, which is amorphous and about 20–30 nm in thickness. The content of TiO_2 nanocrystals in the nanocomposite is about 31.1 wt.%. This $\text{TiO}_2@\text{C}$ anode shows stable cyclability and retains a good reversible capacity of 400 mAh g^{-1} after 100 cycles at a current density of about 100 mA g^{-1} , owing to the enhanced conductivity and protection of carbon shell.

Electronic supplementary material The online version of this article (doi:10.1007/s11581-017-2053-6) contains supplementary material, which is available to authorized users.

Keywords Solid-phase synthesis · Core-shell structure · TiO_2 nanocrystals · Lithium-ion battery

✉ Boyang Liu
byliu@shmtu.edu.cn

Yingfeng Shao
shaoyf@lnm.imech.ac.cn

Xin Xiang
2243366720@qq.com

Jiayuan Ren
782243519@qq.com

Wenge Li
wgli@shmtu.edu.cn

Introduction

Nowadays, lithium-ion batteries (LIBs) have been generally accepted as power sources for consumer electronics and electric/hybrid electric-vehicles because of their merits in terms of high energy density, long cycle life, tiny memory effect, low toxicity, and cost [1–3]. The battery performance is depending on the intrinsic characteristics of electrode material, and commercial carbonaceous anodes show an increased resistance at high rate, which is inappropriate for advanced high-power LIBs in future [4]. Therefore, a lot of efforts have been made for developing various candidates with different nanostructures and physicochemical properties to improve the battery performance. Titanium dioxide (TiO_2) is a widely used material in industrial applications because of its abundance, relatively low price, nontoxicity, and excellent stability [5]. Most TiO_2 polymorphs (including rutile, anatase, and brookite) and their hybrids are regarded as attractive options for

¹ College of Ocean Science and Engineering, Shanghai Maritime University, Shanghai 201306, China

² State Key Laboratory of Nonlinear Mechanics, Institute of Mechanics, Beijing 100190, China

³ Merchant Marine College, Shanghai Maritime University, Shanghai 201306, China

lithium storage owing to their superior inherent safety and chemical compatibility with the electrolyte [6]. Compared with carbon anodes, TiO_2 exhibits a comparable theoretical capacity of 335 mAh g^{-1} according to the accommodation of one Li per TiO_2 [7]. It also has a higher voltage in the range of 1.5–1.8 V relative to lithium depending on different polymorphs, thus preventing the formation of lithium dendrites and side reactions between the electrode and electrolyte [8]. Furthermore, its volume expansion is only about 3.7% within the crystalline lattice upon lithium insertion/extraction, rendering the incredible stability under long and high-rate cycling [9]. However, both of the lithium-ion diffusivity and electronic conductivity of TiO_2 are relatively low, which can adversely affect the rate capability of LIBs [10]. To address the negative issues, TiO_2 in various nanocrystalline forms are widely used to reduce the diffusion path length for lithium-ions and increase high contact area between electrolyte and electrode, thereby improving both storage capacity and rate capability [11–13]. Another common strategy involves incorporation of TiO_2 with carbonaceous materials, which can enhance the electronic conductivity and suppress the aggregation of TiO_2 nanocrystals, thus increasing the anode stability during cycling [14–16]. Consequently, TiO_2 @carbon nanocomposite is considered as a promising high-performance anode material in LIBs, and several synthesis methods have been developed.

Conventionally, TiO_2 nanomaterials, such as nanoparticles, nanorods, and nanotube arrays, can be obtained by flame spray pyrolysis, sol-gel method, electrochemical anodization, and hydrothermal process [17–20]. Otherwise, carbon nanostructures are mainly fabricated by self-recombination of carbon clusters through physical evaporation of graphite, chemical pyrolysis of organic precursors, and hydrothermal carbonization of carbohydrate sources in different temperature ranges [21–23]. Therefore, TiO_2 and carbon are generally prepared individually and then hybridized because of their different formation mechanisms and incompatible starting materials. For example, Oh et al. first synthesized TiO_2 spheres using TiCl_4 as the precursor by hydrothermal method at 120°C for 24 h, which were then mixed with sucrose in a solution. Carbon coating was further obtained by annealing of the homogeneous mixture at 400°C in Ar atmosphere [24]. Wang et al. prepared TiO_2 hollow nanospheres using monodisperse silica spheres as templates, and then, a resorcinol-formaldehyde layer was coated on these spheres, which subsequently turned to carbon shell under Ar atmosphere at 700°C [25]. It is also a common strategy to grow TiO_2 nanomaterials on the high-performance carbon nanotubes and graphenes by hydrothermal method [26–28]. However, it is evident that multi-step, long reaction time and high temperature are usually required for preparation of TiO_2 @carbon nanocomposites. Additionally, it is difficult to ensure controllable and homogeneous distribution of the nanosized TiO_2 and carbon in scalable synthesis, which may lead to the unsatisfied

rate capability and cycling performance of the LIBs. Consequently, it is still an ongoing issue to explore simple, efficient, high yield, and environmentally friendly preparation techniques on the basis of new formation mechanism for overcoming the shortcomings of current methods.

In the present work, a novel solid-phase reaction between titanium metallocene and ammonium persulfate ($(\text{NH}_4)_2\text{S}_2\text{O}_8$, abbreviated as APS) has been developed for in situ one-step preparation of carbon-encapsulated TiO_2 nanocrystals (TiO_2 @C) with core-shell structure at 200°C . TiO_2 @C with homogeneous morphology exhibits high specific capacity and rate capability, as well as excellent cycling stability.

Experimental

Materials and preparation

All the chemicals were received as analytical reagent grade and used without further purification. Four titanium metallocenes, including bis(cyclopentadienyl)titanium dichloride ($(\text{C}_5\text{H}_5)_2\text{TiCl}_2$, abbreviated as Cp_2TiCl_2), bis(cyclopentadienyl)dicarbonyl titanium ($\text{Cp}_2\text{Ti}(\text{CO})_2$), cyclopentadienyltitanium trichloride (CpTiCl_3), and cyclopentadienyl(cycloheptatrienyl)titanium ($\text{CpTi}(\text{C}_7\text{H}_7)$), were used to react with APS in an autoclave at 200°C with an identical process, respectively. Taking sample #1 for example, 4 mmol of $\text{Cp}_2\text{Ti}_2\text{Cl}_2$ and 8 mmol of APS were weighed and manually milled by an agate mortar. Then, the homogeneously mixed reactants were sealed in an autoclave with a 50-ml PTFE liner and held at 200°C in an electric heat oven for 30 min. After the reaction, the as-prepared powder was thoroughly rinsed with deionized water and ethanol in sequence to remove the soluble by-products, and TiO_2 @C was eventually obtained after being dried in a vacuum oven at 100°C . Other samples were also prepared by different precursors which can affect the morphology and microstructure of the products (Table 1).

Characterization

Phase structures of the samples were characterized by X-ray diffraction (XRD) using a PANalytical X'Pert PRO diffractometer with $\text{Cu K}\alpha$ radiation. Raman spectrum of the samples was recorded by a Bruker Senterra micro Raman spectrometer with an excitation wavelength of 633 nm at 2 mW. The surface morphology, microstructure, and composition of the samples were analyzed by field-emission scanning electron microscopy (SEM, JEOL JSM 7500F) and transmission electron microscopy (TEM, JEOL JEM 2010) equipped with an X-ray energy-dispersive spectroscopy system (EDS, EDAX). The reaction behaviors of the reactants and the final product of sample #1 in ambient atmosphere were determined by

Table 1 Synthesis parameters of carbon and TiO₂ nanocomposites

No.	Reactants				Vol. of autoclave (ml)	Temp. (°C)	Time (min)	Major products
	Titanium metallocenes	mmol	Ammonium persulfate	mmol				
#1	(C ₅ H ₅) ₂ TiCl ₂	4	(NH ₄) ₂ S ₂ O ₈	8	50	200	30	TiO ₂ @C
#2	(C ₅ H ₅) ₂ Ti(CO) ₂	4		8				Carbon, S ₈ and TiO ₂
#3	(C ₅ H ₅)TiCl ₃	4		8				Carbon and TiO ₂
#4	(C ₅ H ₅)Ti(C ₇ H ₇)	4		8				TiO ₂ @C

differential scanning calorimetry and thermogravimetric analysis (DSC-TG, Netzsch STA 449F3) using open pans, respectively. The DSC of the reactants in a sealed aluminum pan was also carried out on a Netzsch DSC 204F1 to simulate the reactions of sample #1 in autoclave. The Brunauer-Emmett-Teller (BET) surface area and Barrett-Joyner-Halenda (BJH) pore size distribution of sample #1 were calculated from the adsorption branch of the nitrogen isotherms at 77 K on a Micromeritics ASAP 2020 porosimeter.

Electrochemical measurements

For the fabrication of working electrodes, TiO₂@C (sample #1), acetylene black and polyvinylidene fluoride (PVDF) in a weight ratio of 80:10:10 were evenly mixed in N-methyl-2-pyrrolidone (NMP) solvent. The as-prepared slurry was coated on a thin copper foil ($\phi = 14$ mm) and then thoroughly dried in vacuum at 120 °C. The electrochemical tests were conducted by the assembly of coin-type cell in an Ar-filled glove box with lithium foil as the counter electrode separated by a Celgard 2400 microporous polypropylene film. The 1.0 M LiPF₆ solution in a mixture of ethylene carbonate (EC) and dimethyl carbonate (DMC) (1:1 in volume) was used as the electrolyte. The galvanostatic charge/discharge curves of cells were measured on a battery testing system (Neware, BST-5V3mA) between 0.05 and 3 V versus Li/Li⁺ at different current densities. The cyclic voltammogram (CV) was performed on a CHI 630A electrochemical workstation in the voltage range of 1.0–3.0 V and at a scan rate of 0.1 mV s^{−1}.

Results and discussion

For sample #1, after the preparation, the black fluffy powder and soft agglomerates were found in the top and bottom of the autoclave, respectively. These powders could be differentially collected and the corresponding XRD results are shown in Fig. 1a. It indicates that the black fluffy powder is mainly composed of anatase and rutile TiO₂ (indicated by A-TiO₂ and R-TiO₂, respectively). The strong peaks located at $2\theta = 23^\circ$ and 33° correspond to the strongest characteristic

peaks of NH₄Cl, which can be regarded as a main by-product. Another by-product with good crystallinity can be found in the as-prepared bottom sample, and most strong diffraction peaks can be indexed to (NH₄)₃H(SO₄)₂, ascribing to the decomposition of APS. After removal of (NH₄)₃H(SO₄)₂ and NH₄Cl through washing process, the sharp peaks located at $2\theta = 26^\circ$ and 28° can be unambiguously assigned to the strongest characteristic peaks of A-TiO₂ (101) and R-TiO₂ (110), respectively. It should be noted that the phase component of the washed top and bottom power is the same according to the

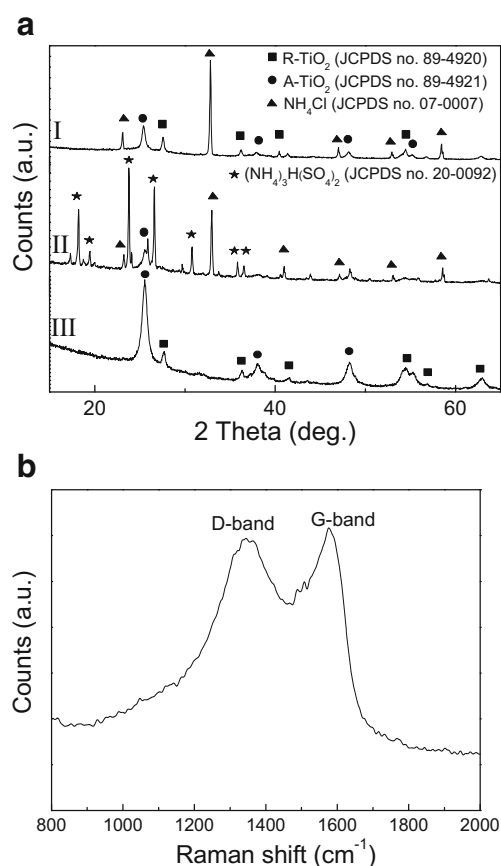


Fig. 1 **a** XRD patterns of the sample #1 in the different position of the autoclave: (I) as-prepared top powder; (II) as-prepared bottom powder; (III) washed bottom powder. **b** Raman spectrum of the washed bottom powder

diffraction peaks. Additionally, the peak of A-TiO₂ (101) is much stronger than R-TiO₂ (110), suggesting that anatase phase is preferentially and abundantly formed during the oxidation of Cp₂TiCl₂. On the other hand, although carbon diffraction peaks are absent in XRD pattern, it can be clearly proved by the two typical D- and G-band Raman shifts located at 1350 and 1580 cm⁻¹, respectively, as shown in Fig. 1b. The relatively high intensity D-band peak confirms that amorphous carbon with lattice distortion is obtained because the low synthesis temperature is not beneficial to the formation of graphitizable carbon.

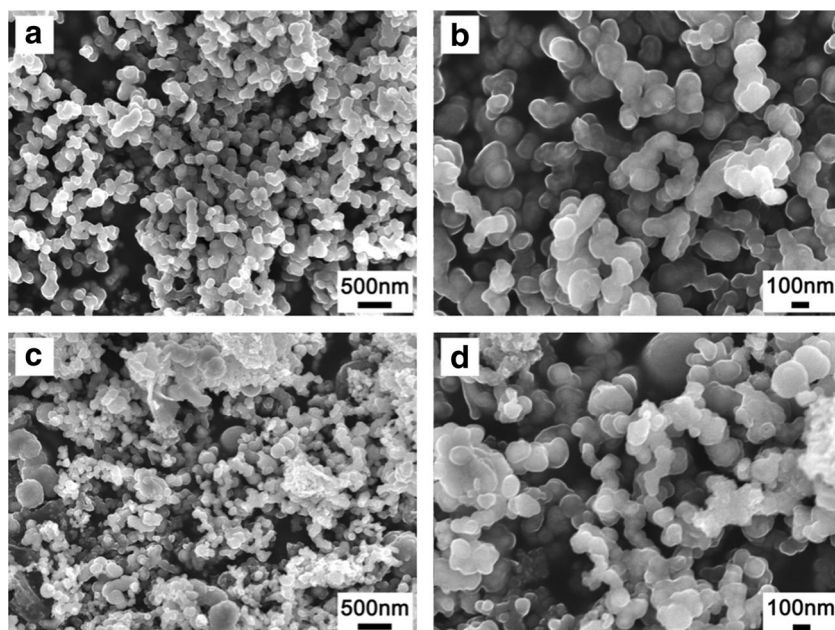
The low magnification SEM image of the TiO₂@C in sample #1 in Fig. 2a shows that the sample has a uniform morphology and consists of equiaxed nanoparticles. It is distinct that the nanoparticles have a typical diameter about 100 nm and aggregate together. At high magnification, these nanoparticles obviously show core-shell structure composed of white cores inside and an exterior semitransparent thin layer, corresponding to TiO₂ nanocrystals and carbon shell (Fig. 2b). Moreover, the carbon layer encapsulates lots of TiO₂ nanocrystals as a whole, rather than separately and individually encapsulates each nanocrystal. The morphology of the bottom powder is almost the same as the top powder and core-shell structure is clearly revealed (Fig. 2c, d), demonstrating that the solid-phase synthesis is very simple and effective to yield highly homogeneous product.

The TEM images can provide further details on the morphology and microstructure of TiO₂@C in sample #1. In Fig. 3a, it can be seen that the white inner cores under the carbon layer in SEM image are actually the agglomerated small nanocrystals. The worm-like carbon shell about 20–30 nm in thickness is interconnected and encapsulates

hundreds of nanocrystals inside, exhibiting a uniform core-shell structure. Figure 3b, c shows that high-resolution TEM images of carbon encapsulated some typical equiaxed nanocrystals. The carbon shell is further proved to be amorphous according to its disordered lattice fringes. On the other hand, the two-dimensional lattice fringes in the two nanocrystals can be well indexed to anatase TiO₂ (101) and rutile TiO₂ (110) and (200) planes, respectively. The nanocrystal size is accurately measured in several TEM images, and the nanocrystals have a small size of 10–55 nm according to the histogram (Fig. 3d), where the median size is 30.3 nm. From tens of SEM and TEM images, it is found that all the TiO₂ nanocrystals are perfectly and homogeneously encapsulated by carbon. Despite that the solid-phase based synthesis is very simple, the morphology and quality of TiO₂@C can be effectively guaranteed.

The DSC-TG analysis conducted in air atmosphere is used to evaluate the composition of TiO₂@C in sample #1. The weight loss between 400 and 600 °C in the TG curve is accompanied by a strong exothermic peak in the DSC curve, implying that the exterior carbon shell is burned off during this stage (Fig. 4a). After 600 °C, the oxidation of TiO₂@C is completed, and the TG curve shows a steady plateau with a residue of 31.1% of the initial mass, corresponding to the content of TiO₂ nanocrystals in the TiO₂@C. The relatively low content of TiO₂ implies that the carbon shell is thick compared to the fine nanocrystals, which is in accordance with the TEM images. However, the theoretical content of TiO₂ in the nanocomposite should be 40% on condition that the Cp ligand and Ti atom in Cp₂TiCl₂ completely transform to carbon and TiO₂, respectively. Thus, it is assumed that a small amount of soluble titanium-containing by-product is

Fig. 2 SEM images of the sample #1 in the different position of the autoclave. **a, b** Top powder. **c, d** Bottom powder



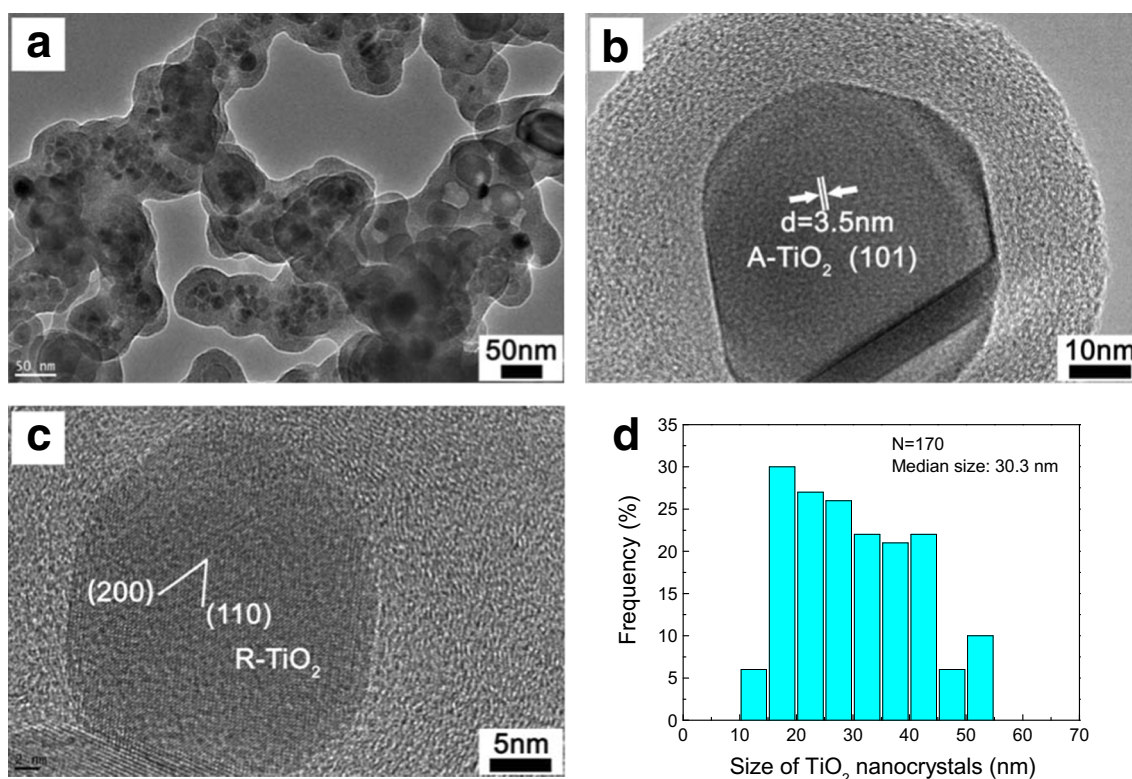


Fig. 3 a–c TEM images of the $\text{TiO}_2\text{@C}$ in sample #1. d Size distribution of TiO_2 nanocrystals

simultaneously formed during the synthesis and subsequently eliminated in the washing process. The nitrogen isotherms, BJH pore size distribution, and BET surface of the $\text{TiO}_2\text{@C}$ are indicated in Fig. 4b. The broad hysteresis loop in the relative pressure range of 0.4–1.0 is associated with the existence of mesopores, and the upward curvature at the relative pressure higher than 0.8 corresponds to the cylindrical mesopores [29]. However, the total pore volume of the $\text{TiO}_2\text{@C}$ should be small according to the low adsorbing capacity under the pressure of 0.4. The BJH pore size distribution reveals that the pores less than 10 nm are dominant in the sample. Otherwise, the low BET surface area of $\text{TiO}_2\text{@C}$ ($80.2 \text{ m}^2 \text{ g}^{-1}$) illustrates that carbon shell and TiO_2 cores are in close contact with each other, which is consistent with the TEM images.

Figure 5a shows the DSC-TG curves of the pure APS and the mixture of Cp_2TiCl_2 and APS in sample #1 in open alumina pans, respectively. It is obvious that the pure APS will exothermically decompose at about 190°C to create oxygen [30]. When Cp_2TiCl_2 is added, the reaction temperature is distinctly reduced to 174°C (onset point), and the mixture suffers a much stronger exothermic reaction than pure APS according to the intensive peak in the DSC curve. Meanwhile, the sample weight instantaneously loses 25.3% of the initial mass based on the TG curve, which should be caused by the release of generated gases. After that, the sample weight slowly decreases with the increment of temperature. These phenomena imply that an explosive reaction takes place between

the two solid reactants and a large amount of heat and gases are generated. With the purpose of simulating the reaction behavior in autoclave, the DSC analyses of the reactants in sealed aluminum pans are further carried out, as shown in Fig. 5b. A small new exothermic peak is revealed around 150°C for pure APS, and it is probably due to the existence of a tiny moist air sealed in the pan, which can promote the decomposition of APS. The second peak around 190°C is similar to that in the open pan and slightly shifts to the low temperature region. It can be explained that the decomposition products sealed in the reactor can further accelerate the reaction. When Cp_2TiCl_2 is introduced, the initial peak at 150°C is attributed to the decomposition of APS under the residual moist air and the subsequent oxidation of Cp_2TiCl_2 . Notably, the dominant peak at 180°C becomes much broader and stronger, corresponding to the spontaneous ignition of Cp_2TiCl_2 and liberation of H_2O and SO_2 (tested after the synthesis). It has been proved that the ammonium and oxidizing ions tend to reduce the stability of metallocene complexes and destroy the ferrocene-like sandwich structure at about 200°C [31–33]. Compared to the reaction in the open pan, lots of heat and gases generated in the process are encapsulated in the sealed pan, quickly rising the temperature and pressure in the reactor. Therefore, the temperature in the autoclave will be much higher than 200°C , and the cyclopentadiene ligands in Cp_2TiCl_2 are cleaved into small carbon fragments, which eventually turn to carbon shell after oxidative

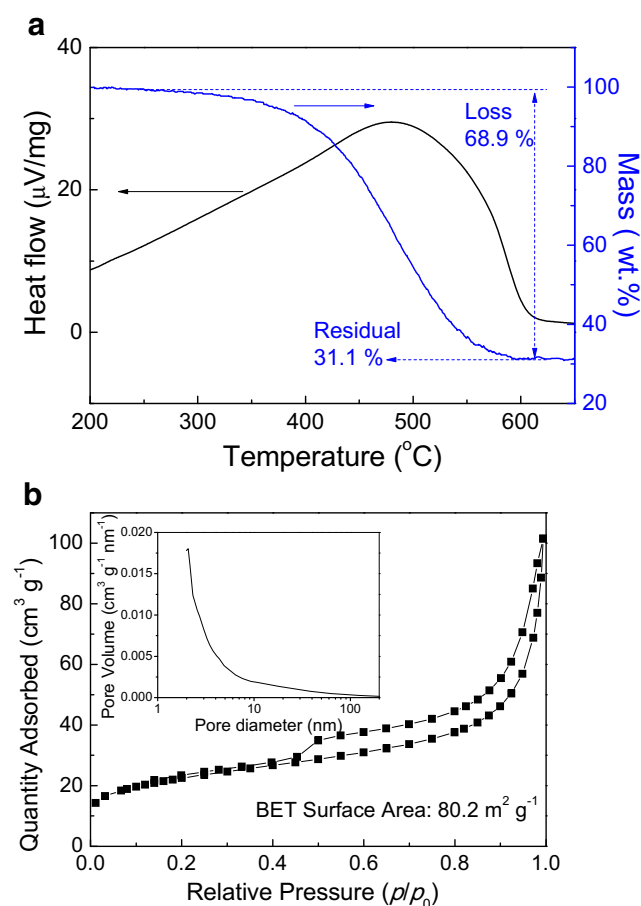


Fig. 4 **a** DSC-TG curve and **b** N_2 isotherms, BET surface area, and BJH pore size distribution of the $TiO_2@C$ in sample #1

dehydrogenation. In addition, the Ti and Cl atoms in Cp_2TiCl_2 will transform to TiO_2 and NH_4Cl , respectively. On the contrary, APS is reduced to SO_2 and $(NH_4)_3H(SO_4)_2$. During the explosive reaction, carbon fragments filled with the autoclave inhibit the grain growth of TiO_2 , resulting in the formation of small TiO_2 nanocrystals. And the π interaction between Ti and carbon fragments should be responsible for the creation of core-shell structure [34–36].

Although the $TiO_2@C$ can be efficiently synthesized in sample #1, multiphase TiO_2 coexist and their total mass is low due to the thick carbon coating. Therefore, the synthesis parameters should be optimized in order to prepare carbon-encapsulated high-content pure phase TiO_2 nanocrystals. According to the thermal analysis above, a very rapid explosive reaction between Cp_2TiCl_2 and APS can liberate an appreciable amount of energy in a short time, thereby producing copious amounts of radicals and atoms which in turn react with each other to form $TiO_2@C$. Consequently, explosive reaction with high energy release is crucial for the formation of core-shell structure, which should be further depending on the molecular structure and property of the starting precursor. It has been confirmed by the following samples using different precursors.

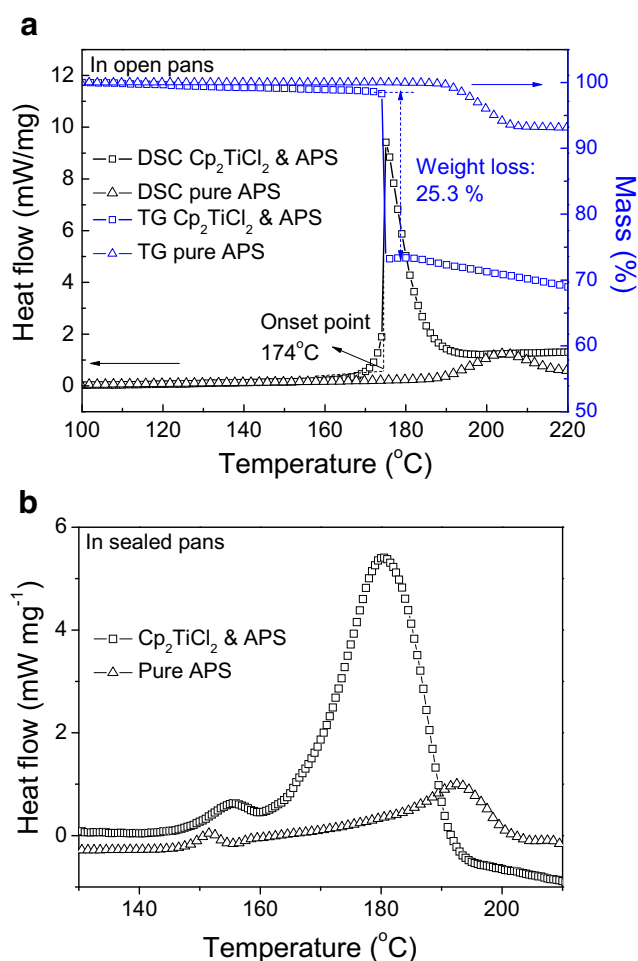
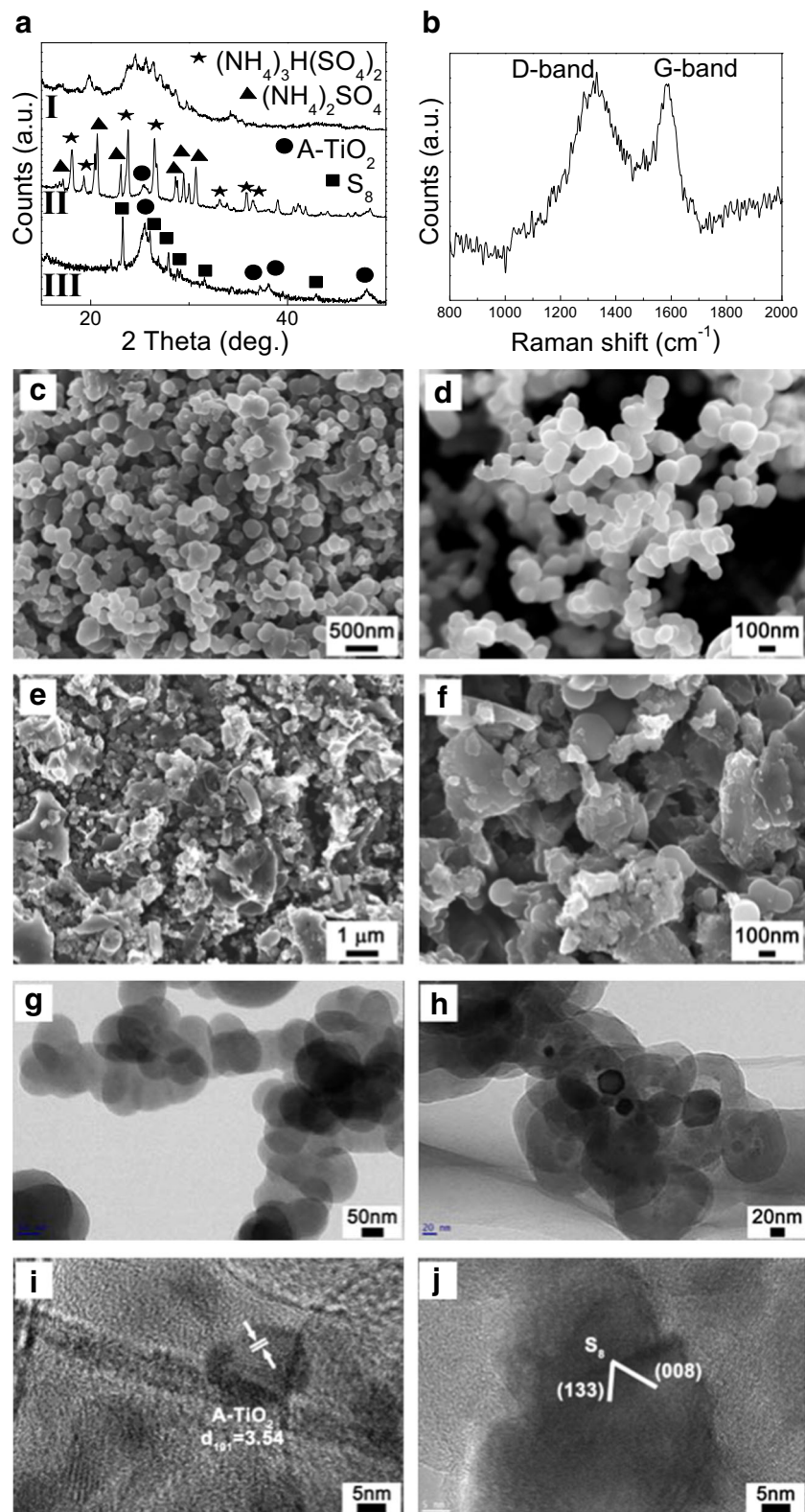


Fig. 5 **a** DSC-TG and **b** DSC of the reactants in sample #1 in open and sealed pans, respectively

It has been demonstrated that NH_4Cl can react with ferrocene to fabricate amorphous carbon in oxidation environment at 200 °C [33], implying that the presence of NH_4Cl may reduce the purity of core-shell structure. Therefore, in sample #2, $Cp_2Ti(CO)_2$ is used as the precursor in which carbonyl groups substitute for the chlorine atoms in order to avoid the formation of NH_4Cl . Figure 6a I shows the XRD pattern of the top powder and only a broad peak can be found, corresponding to the amorphous carbon without nanocrystals inside. The as-prepared bottom powder is abundant of $(NH_4)_3H(SO_4)_2$ and $(NH_4)_2SO_4$ (Fig. 6a II), which is similar to sample #1. After washing, the diffraction peaks of A- TiO_2 and S_8 (JCPDS no. 74-1465) are revealed and the additional generation of S_8 may be attributed to the deep reduction of $(NH_4)_2S_2O_8$ (Fig. 6a III). The high D-band peak in the Raman spectrum of Fig. 6b further illustrates that amorphous carbon is obtained.

The SEM images of the top powder show that the homogeneous interconnected nanoparticles are the major product (Fig. 6c, d). However, no bright cores can be found inside, suggesting that only amorphous carbon is fabricated without

Fig. 6 **a** XRD patterns of the sample #2 in the different position of the autoclave: (I) as-prepared top powder; (II) as-prepared bottom powder; (III) washed bottom powder. **b** Raman spectrum of the washed bottom powder. SEM images of the top (**c, d**) and bottom powder (**e, f**) at different magnification. TEM images of the top (**g**) and bottom powder (**h–j**)



TiO_2 inner cores, which is in accordance with the XRD pattern. The uniformity of the bottom powder is greatly decreased due to the existence of lots of irregularly shaped particles, as shown in Fig. 6e, f. TEM image in Fig. 6g demonstrates that

only worm-like carbon is formed in the top powder. Otherwise, a small amount of carbon-encapsulated TiO_2 and S_8 nanocrystals can be found in the bottom powder, as shown in Fig. 6h–j.

It is deduced that the carbonyl groups can suppress the explosive reaction between $\text{Cp}_2\text{Ti}(\text{CO})_2$ and $(\text{NH}_4)_2\text{S}_2\text{O}_8$ and the released power is reduced. Therefore, only a small amount of Cp ligands are torn into carbon fragments, and then pushed up by the produced gas stream to form worm-like carbon nanoparticles. On the other hand, the $(\text{NH}_4)_3\text{H}(\text{SO}_4)_2$ and $(\text{NH}_4)_2\text{SO}_4$ decomposed from $(\text{NH}_4)_2\text{S}_2\text{O}_8$ are deposited at the bottom. These ammonium sulfates are similar to NH_4Cl and also reactive to $\text{Cp}_2\text{Ti}(\text{CO})_2$, mainly forming irregularly shaped amorphous carbon particles. Though $(\text{NH}_4)_3\text{H}(\text{SO}_4)_2$ is also present in sample #1, the rapid explosive reaction is dominant rather than other side reactions, thus leading to the formation of homogeneous core-shell structure.

As discussed above, the carbon content of $\text{TiO}_2@\text{C}$ is low in sample #1, which is depending on the atomic ratio of carbon to Ti in the precursor. Therefore, in sample #3, CpTiCl_3 is used to increase the content of TiO_2 by the reduction of carbon atom in the precursor. After the reaction, all the powder is found at the bottom of the autoclave. Figure 7a I shows the XRD pattern of the as-prepared product, which is primarily composed of NH_4Cl like to sample #1. After washing, only A- TiO_2 is remained, demonstrating that CpTiCl_3 is appropriate

for preparation of pure phase TiO_2 (Fig. 7a II). The Raman spectrum in Fig. 7b proves that carbon is also amorphous owing to the low synthesis temperature. However, large amount of irregularly shaped particles are formed instead of core-shell structure, as shown in SEM images (Fig. 7c, d). TEM observations further display that amorphous carbon and A- TiO_2 nanocrystals are aggregated together (Fig. 7e, f). Considering that the power of explosive reaction is determined by the amount of Cp ligand and $(\text{NH}_4)_2\text{S}_2\text{O}_8$, the decline of Cp ligand number in the precursor will greatly weaken the explosive reaction, resulting in the formation of inhomogeneous product without core-shell structure. Otherwise, compared with the first two samples, the small quantity of heat released during the explosive reaction may be beneficial for the synthesis of pure phase TiO_2 .

$\text{CpTi}(\text{C}_7\text{H}_7)$ is chosen in sample #4, and the influence of Cl atom or carbonyl group on the synthesis can be eliminated. Besides A- TiO_2 and R- TiO_2 , S_8 appears in the top powder due to the deep reduction of $(\text{NH}_4)_2\text{S}_2\text{O}_8$, as shown in the XRD pattern (Fig. 8a I). $(\text{NH}_4)_3\text{H}(\text{SO}_4)_2$ is similarly found in the as-prepared bottom powder, and A- TiO_2 and R- TiO_2 are eventually obtained after washing process (Fig. 8a II and III). The

Fig. 7 **a** XRD patterns of the sample #3 in the bottom of the autoclave: (I) as-prepared powder; (II) washed powder. **b** Raman spectrum of the washed powder. **c, d** SEM and **e, f** TEM images of the bottom powder at different magnification

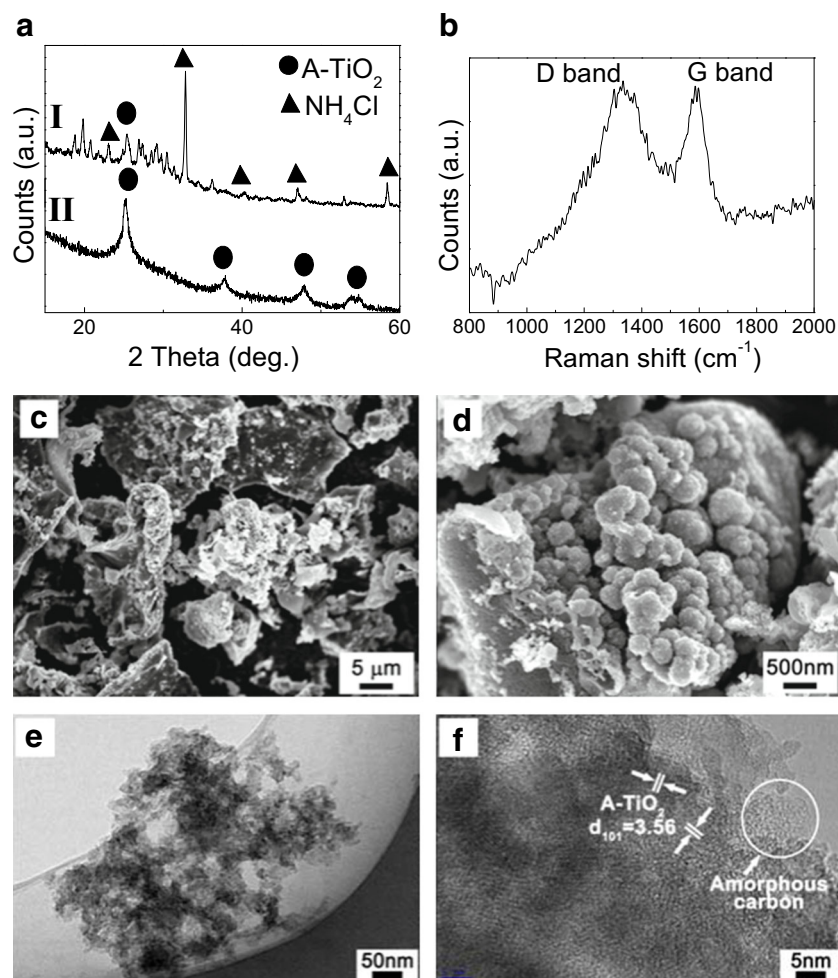
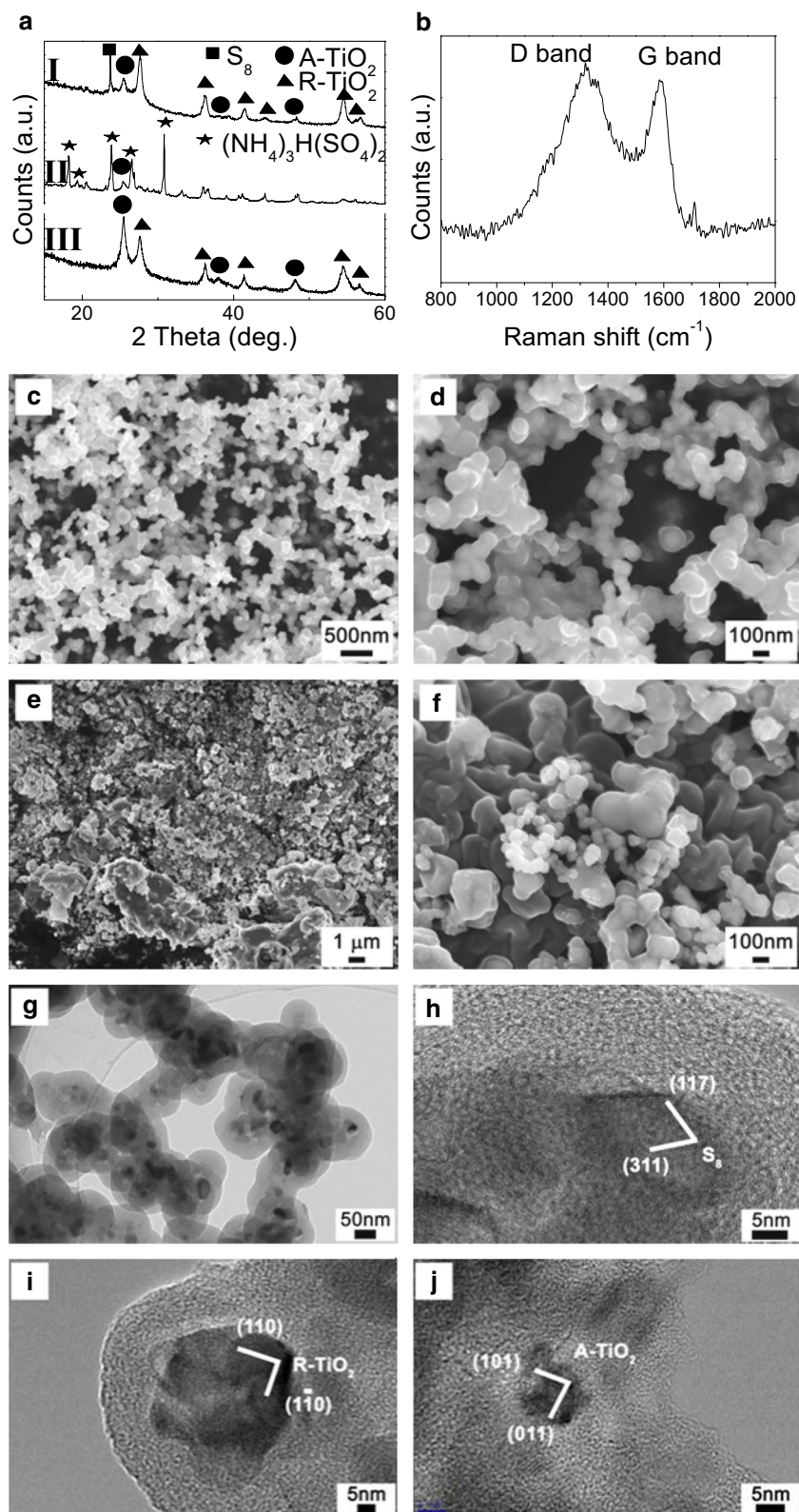


Fig. 8 **a** XRD patterns of the sample #4 in the different position of the autoclave: (I) as-prepared top powder; (II) as-prepared bottom powder; (III) washed bottom powder. **b** Raman spectrum of the washed bottom powder. SEM images of the top (c, d) and bottom powder (e, f) at different magnification. Large domain TEM image of the core-shell structure (g) and the two-dimensional lattice images of nanocrystals (h–j) in the top powder



carbon is amorphous as well according to the Raman spectrum (Fig. 8b). The top powder has a homogeneous morphology composed of interconnected nanoparticles with obvious inner cores (Fig. 8c, d). The washed bottom powder also shows a

good uniformity of core-shell structure, which is identical with sample #1 (Fig. 8e, f). The core-shell structure, amorphous carbon shell, as well as different types of nanocrystals can be distinctly revealed in the TEM images (Fig. 8g–j).

Consequently, $\text{CpTi}(\text{C}_7\text{H}_7)$ is suitable for preparation of homogeneous core-shell structure, but the carbon content of the product should be higher than other samples because of the more carbon atoms in the precursor.

Based on the discussion above, the explosive reaction is important for the synthesis of homogeneous $\text{TiO}_2@\text{C}$ with core-shell structure. The released heat during the reaction should not only be high enough to cleave the Cp ligands, but also not too much for pure phase A- TiO_2 . Additionally, the precursor without Cl atom or carbonyl groups bound with Ti atom is an ideal selection to avoid side reactions. Nevertheless, commercial titanocene complexes are comparatively few, and further, more detailed investigation should be carried out on these specific aspects.

The $\text{TiO}_2@\text{C}$ in sample #1 is taken as anode for Li-ion battery because of its homogeneous core-shell structure. Figure 9a displays the first three CV cycle profiles for $\text{TiO}_2@\text{C}$ anode at a scan rate of 0.1 mV s^{-1} in the voltage range of 1.0–3.0 V. A major pair of cathodic/anodic peaks for Li intercalation/deintercalation is observed at 1.7 and 2.0 V, respectively, in accordance with the pair of peaks in the mixture of A-/R- TiO_2 [37]. Another pair of broad peaks (at 1.45 and 1.75 V) associated with differing site occupations might be attributed to the formation of the discrete phase or

imperfection of the TiO_2 lattice, which facilitate the transport of Li through surface defects and in bulk materials [16].

The content of TiO_2 is low and carbon shell is the dominant phase in sample #1. Therefore, the electrochemical performance of $\text{TiO}_2@\text{C}$ anode was measured between 0.01 and 3 V. The charge/discharge profiles in Fig. 9b demonstrate that the $\text{TiO}_2@\text{C}$ anode possesses an initial discharge and charge capacity of 993 and 653 mAh g^{-1} , respectively, corresponding to an irreversible capacity loss of 34% due to the formation of solid electrolyte interphase (SEI) film on the carbon shell. For pure TiO_2 anode, the capacity is usually measured in the voltage of 1.0–3.0 V, in which range in the capacity of amorphous carbon can be negligible [38]. Hence, the capacity of TiO_2 nanocrystals in the nanocomposite is roughly estimated to be 183 mAh g^{-1} in the second cycle. The voltage profile of $\text{TiO}_2@\text{C}$ in the second discharge process shows three distinct regions at 1–3 V. Region 1 ranging from open circuit voltage (OCV) to 1.75 V shows a rapid voltage drop, which is known as a homogeneous Li^+ insertion into the bulk by a solid-solution insertion mechanism. A well-known two-phase plateau in region 2 is observed at 1.5–1.75 V, where Li-rich phases and Li-poor phases coexist. After the two-phase plateau, the region 3 below 1.5 V exhibits a sloped curve. This process can be attributed to the reversible surface/interfacial

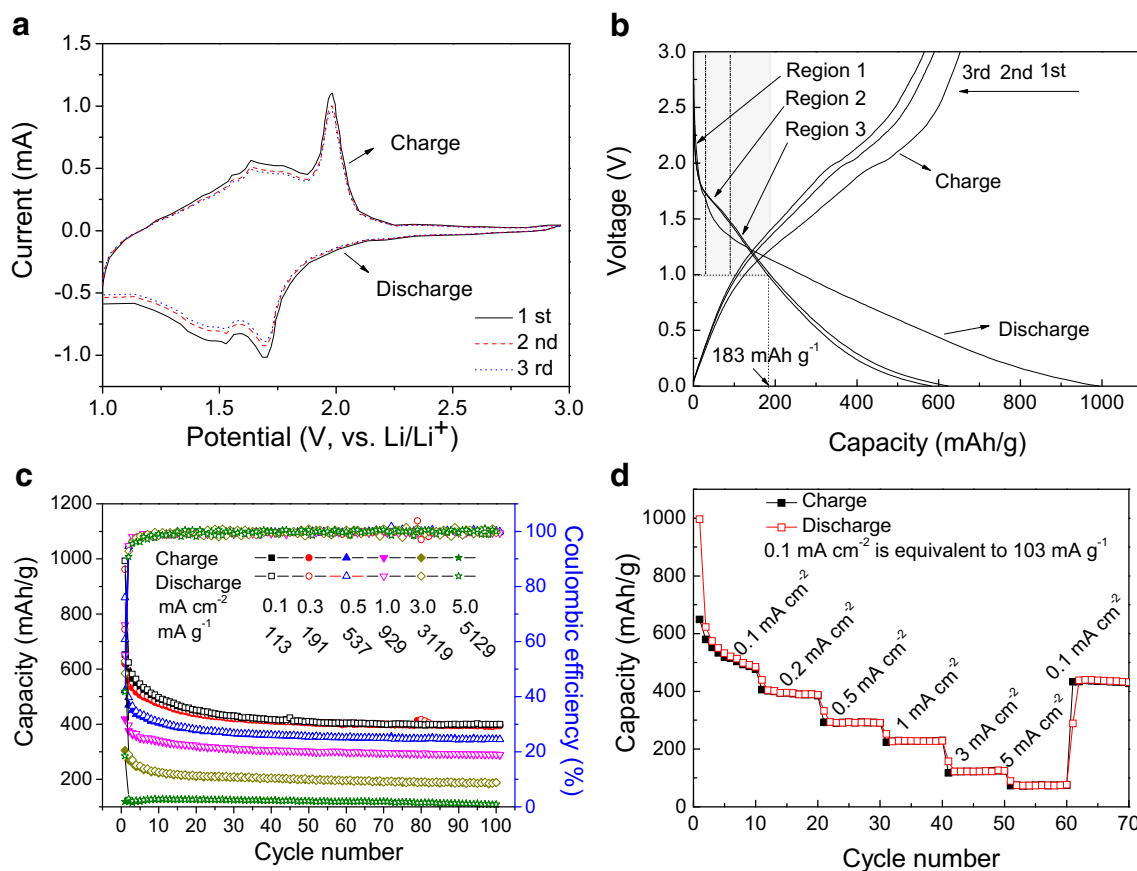


Fig. 9 Electrochemical performances of $\text{TiO}_2@\text{C}$ in sample #1. **a** Cyclic voltammograms at a scan rate of 0.1 mV s^{-1} . **b** The charge/discharge curves at a current density of 0.1 mA cm^{-2} . **c** Cycling stability and Coulombic efficiency. **d** Rate performance

lithium storage on the TiO_2 and carbon, which is consistent with the CV shown in Fig. 9a.

The cycling stability and Coulombic efficiency of $\text{TiO}_2@\text{C}$ anodes at various current densities are exhibited in Fig. 9c. The $\text{TiO}_2@\text{C}$ anode shows good capacity retention during the 100 successive cycles at 0.1 mA cm^{-2} (113 mA g^{-1}) and still maintains a high reversible capacity of 400 mAh g^{-1} with respect to commercial graphite anode. When the current density is elevated, a high reversible capacity of 394, 345, 288, 188, and 109 mAh g^{-1} after 100 cycles can be obtained at 0.2, 0.5, 1.0, 3.0, and 5.0 mA cm^{-2} (about 5 A g^{-1}), respectively. The $\text{TiO}_2@\text{C}$ retains a good capacity because of the entire carbon encapsulation and the stable core-shell structure. The Coulombic efficiencies rapidly increase to about 98% in the fifth cycle and are well maintained around 100% in the following cycles, illustrating that the small TiO_2 nanocrystals enable the facile transport of lithium-ions and electrons in the nanocomposite. The rate capability of $\text{TiO}_2@\text{C}$ is investigated by stepwise increasing the current density for every 10 cycles from 0.1 to 5.0 mA cm^{-2} and then returning back (Fig. 9d). The $\text{TiO}_2@\text{C}$ anode shows outstanding high rate performance with a small decline in capacity as the current density increases. Remarkably, when the current density decreases from 5.0 to 0.1 mA cm^{-2} , the capacity of $\text{TiO}_2@\text{C}$ anode returns from 75 to 289 mAh g^{-1} at once and further increases to a stable stage of 431 mAh g^{-1} , implying that the anode is highly stable and reversible.

The discharge capacities of several $\text{TiO}_2@\text{C}$ anodes in the voltage of 1–3 V are also simply summarized in Table S1 (Supplementary Material). The capacity is not only depending on the morphology and microstructure of the nanocomposite, but also the amount of carbon incorporation. Compared to the TiO_2 -rich anode, the relatively low capacity of $\text{TiO}_2@\text{C}$ is mostly ascribed to the small content of TiO_2 in the nanocomposite. Moreover, the excessively thick carbon coating on TiO_2 nanocrystals will act as a barrier for Li^+ diffusion, which decreases the rate performance. Consequently, controllable incorporation of a small amount of thin carbon shell into fine TiO_2 nanocrystals should be further investigated for high-performance $\text{TiO}_2@\text{C}$ anode.

Conclusion

A novel and efficient low-temperature solid-phase reaction has been successfully developed for in situ one-step preparation of $\text{TiO}_2@\text{C}$ with core-shell structure. The rapid generation of a large amount of heat in the autoclave cleaves the cyclopentadiene ligands into small carbon fragments, which form carbon shell after oxidative dehydrogenation coating on the TiO_2 nanocrystals, resulting in the formation of core-shell structure. In sample #1, the median size of the small equiaxed TiO_2 nanocrystals is 30.3 nm and the thickness of amorphous

carbon shell is 20–30 nm. The $\text{TiO}_2@\text{C}$ anode shows good capacity and stable cyclability at fast charge/discharge rate owing to the good conductivity and protection of carbon shell.

Acknowledgements This work is sponsored by Natural Science Foundation of Shanghai (14ZR1419400, 15ZR1420500), National Natural Science Foundation of China (11572326), Opening fund of State Key Laboratory of Nonlinear Mechanics, and Technology Innovation Action of Shanghai (12nm0503100).

References

- Jiang F, Yang L, Tian Y, Yang P, Hu S, Huang K, Wei X, Zhong J (2014) Bi-component MnO/ZnO hollow microspheres embedded in reduced graphene oxide as electrode materials for enhanced lithium storage. *Ceram Int* 40(3):4297–4304
- Sasaki T, Ukyo Y, Novák P (2013) Memory effect in a lithium-ion battery. *Nature Mater* 12(6):569–575
- Mancini M, Nobili F, Tossici R, Wohlfahrt-Mehrens M, Marassi R (2011) High performance, environmentally friendly and low cost anodes for lithium-ion battery based on TiO_2 anatase and water soluble binder carboxymethyl cellulose. *J Power Sources* 196(22):9665–9671
- Kubiak P, Fröschl T, Hüsing N, Hörmann U, Kaiser U, Schiller R, Weiss CK, Landfester K, Wohlfahrt-Mehrens M (2011) TiO_2 anatase nanoparticle networks: synthesis, structure, and electrochemical performance. *Small* 7(12):1690–1696
- Chen J, Qian Y, Wei X (2010) Comparison of magnetic-nanometer titanium dioxide/ferriferous oxide ($\text{TiO}_2/\text{Fe}_3\text{O}_4$) composite photocatalyst prepared by acid-sol and homogeneous precipitation methods. *J Mater Sci* 45(22):6018–6024
- Yang Z, Choi D, Kerisit S, Rosso KM, Wang D, Zhang J, Graff G, Liu J (2009) Nanostructures and lithium electrochemical reactivity of lithium titanates and titanium oxides: a review. *J Power Sources* 192(2):588–598
- Xue W, Shi X, Xia H (2016) Ultrafine Fe_2O_3 Nanoflakes grafted on TiO_2 Nanosheet arrays as advanced anodes for lithium-ion batteries. *Sci Adv Mater* 8(6):1293–1297
- Wen W, Wu J-m, Jiang Y-z, Yu S-l, Bai J-q, Cao M-H, Cui J (2015) Anatase TiO_2 ultrathin nanobelts derived from room-temperature-synthesized titanates for fast and safe lithium storage. *Sci Rep* 5:11804
- Zhang X, Aravindan V, Kumar PS, Liu H, Sundaramurthy J, Ramakrishna S, Madhavi S (2013) Synthesis of TiO_2 hollow nanofibers by co-axial electrospinning and its superior lithium storage capability in full-cell assembly with olivine phosphate. *Nano* 5(13):5973–5980
- Zhu G, Wang Y, Xia Y (2012) Ti-based compounds as anode materials for Li-ion batteries. *Energy Environ Sci* 5(5):6652–6667
- Han H, Song T, Lee E-K, Devadoss A, Jeon Y, Ha J, Chung Y-C, Choi Y-M, Jung Y-G, Paik U (2012) Dominant factors governing the rate capability of a TiO_2 nanotube anode for high power lithium ion batteries. *ACS Nano* 6(9):8308–8315
- Shin JY, Samuelis D, Maier J (2011) Sustained lithium-storage performance of hierarchical, Nanoporous anatase TiO_2 at high rates: emphasis on interfacial storage phenomena. *Adv Funct Mater* 21(18):3464–3472
- Song T, Han H, Choi H, Lee JW, Park H, Lee S, Park WI, Kim S, Liu L, Paik U (2014) TiO_2 nanotube branched tree on a carbon nanofiber nanostructure as an anode for high energy and power lithium ion batteries. *Nano Res* 7(4):491–501

14. Shen L, Zhang X, Li H, Yuan C, Cao G (2011) Design and tailoring of a three-dimensional TiO₂–graphene–carbon nanotube nanocomposite for fast lithium storage. *J Phys Chem Lett* 2(24):3096–3101
15. Ryu M-H, Jung K-N, Shin K-H, Han K-S, Yoon S (2013) High performance N-doped mesoporous carbon decorated TiO₂ nanofibers as anode materials for lithium-ion batteries. *J Phys Chem C* 117(16):8092–8098
16. Lee DH, Park JG, Jin Choi K, Choi HJ, Kim DW (2008) Preparation of brookite-type TiO₂/carbon nanocomposite electrodes for application to Li ion batteries. *Eur J Inorg Chem* 2008(6):878–882
17. Paulauskas IE, Modeshia DR, Ali TT, El-Mossalamy EH, Obaid AY, Basahel SN, Al-Ghamdi AA, Sartain FK (2013) Photocatalytic activity of doped and undoped titanium dioxide nanoparticles synthesised by flame spray pyrolysis. *Platin Met Rev* 57(1):32–43
18. Macwan D, Dave PN, Chaturvedi S (2011) A review on nano-TiO₂ sol–gel type syntheses and its applications. *J Mater Sci* 46(11):3669–3686
19. Lei B-X, Luo Q-P, Sun Z-F, Kuang D-B, Su C-Y (2013) Fabrication of partially crystalline TiO₂ nanotube arrays using 1, 2-propanediol electrolytes and application in dye-sensitized solar cells. *Adv Powder Technol* 24(1):175–182
20. Ye M, Liu HY, Lin C, Lin Z (2013) Hierarchical rutile TiO₂ flower cluster-based high efficiency dye-sensitized solar cells via direct hydrothermal growth on conducting substrates. *Small* 9(2):312–321
21. Prasek J, Drbohlavova J, Chomoucka J, Hubalek J, Jasek O, Adam V, Kizek R (2011) Methods for carbon nanotubes synthesis—review. *J Mater Chem* 21(40):15872–15884
22. Wang Y, Zheng Y, Xu X, Dubuisson E, Bao Q, Lu J, Loh KP (2011) Electrochemical delamination of CVD-grown graphene film: toward the recyclable use of copper catalyst. *ACS Nano* 5(12):9927–9933
23. Hu B, Wang K, Wu L, Yu SH, Antonietti M, Titirici MM (2010) Engineering carbon materials from the hydrothermal carbonization process of biomass. *Adv Mater* 22(7):813–828
24. Oh S, Hwang J, Yoon C, Lu J, Amine K, Belharouak I, Sun Y (2014) High electrochemical performances of microsphere C-TiO₂ anode for sodium-ion battery. *ACS Appl Mater Interfaces* 6(14):11295–11301
25. Wang W, Sa Q, Chen J, Wang Y, Jung H, Yin Y (2013) Porous TiO₂/C nanocomposite shells as a high-performance anode material for lithium-ion batteries. *ACS Appl Mater Interfaces* 5(14):6478–6483
26. Perera SD, Mariano RG, Vu K, Nour N, Seitz O, Chabal Y, Balkus KJ Jr (2012) Hydrothermal synthesis of graphene-TiO₂ nanotube composites with enhanced photocatalytic activity. *ACS Catal* 2(6):949–956
27. Yang M-Q, Zhang N, Xu Y-J (2013) Synthesis of fullerene-, carbon nanotube-, and graphene-TiO₂ nanocomposite photocatalysts for selective oxidation: a comparative study. *ACS Appl Mater Interfaces* 5(3):1156–1164
28. Sun X, Xie M, Travis JJ, Wang G, Sun H, Lian J, George SM (2013) Pseudocapacitance of amorphous TiO₂ thin films anchored to graphene and carbon nanotubes using atomic layer deposition. *J Phys Chem C* 117(44):22497–22508
29. Janssen AH, Schmidt I, Jacobsen CJH, Koster AJ, de Jong KP (2003) Exploratory study of mesopore templating with carbon during zeolite synthesis. *Micropor Mesopor Mater* 65(1):59–75
30. Erdey L, Gál S, Liptay G (1964) Thermoanalytical properties of analytical-grade reagents. *Talanta* 11(6):913–940
31. Liu B, Zhong N, Fan C, Zhou Y, Fan Y, Yu S, Zhang F, Dong L, Yin Y (2014) Low temperature synthesis and formation mechanism of carbon encapsulated nanocrystals by electrophilic oxidation of ferrocene. *Carbon* 68:573–582
32. Liu B, Huang H, Zhang F, Zhou Y, Li W, Zhang J (2012) Agglomerates of amorphous carbon nanoparticles synthesized by a solution-phase method. *Mater Lett* 66(1):199–202
33. Liu B, Jia D, Zhou Y, Feng H, Meng Q (2007) Low temperature synthesis of amorphous carbon nanotubes in air. *Carbon* 45(8):1710–1713
34. Boyang L, Chunhua F, Jianwei C, Junhua W, Zepeng L, Jiayuan R, Shuaiqin Y, Lihua D, Wenge L (2016) Low temperature in situ synthesis and the formation mechanism of various carbon-encapsulated nanocrystals by the electrophilic oxidation of metallocene complexes. *Nanotechnology* 27(7):075603
35. Liu B, Fan C, Chen J, Zhou Y, Dong L, Wang J (2015a) Low temperature one-step synthesis of carbon co-encapsulated NiS₂, NiS and S₈ nanocrystals by electrophilic oxidation of nickelocene. *Mater Lett* 142:90–93
36. Liu B, Zhang F, Wu Q, Wang J, Li W, Dong L, Yin Y (2015b) Low temperature synthesis of carbon encapsulated Fe₇S₈ nanocrystals as high performance anode for lithium-ion batteries. *Mater Chem Phys* 151:60–65
37. Shen J, Wang H, Zhou Y, Ye N, Li G, Wang L (2012) Anatase/rutile TiO₂ nanocomposite microspheres with hierarchically porous structures for high-performance lithium-ion batteries. *RSC Adv* 2(24):9173–9178
38. Liu B, Zhou Y, Jia D, Zuo P, Shao Y, Zhang J (2011) Effect of heat treatment temperature on microstructure and electrochemical properties of hollow carbon spheres prepared in high-pressure argon. *B Mater Sci* 34:1707–1714